Ferroelectric/paraelectric superlattices for energy storage

Hugo Aramberri,[1, 2] Natalya S. Fedorova,[1, 2] and Jorge Íñiguez[1, 2, 3]

[1]*Materials Research and Technology Department,*
Luxembourg Institute of Science and Technology,
5 avenue des Hauts-Fourneaux, L-4362 Esch/Alzette, Luxembourg
[2]*Inter-institutional Research Group Uni.lu–LIST on Ferroic Materials, 41 rue du Brill, L-4422 Belvaux, Luxembourg*
[3]*Department of Physics and Materials Science, University of Luxembourg, 41 Rue du Brill, L-4422 Belvaux, Luxembourg*
(Dated: December 3, 2021)

The polarization response of antiferroelectrics to electric fields is such that the materials can store large energy densities, which makes them promising candidates for energy storage applications in pulsed-power technologies. However, relatively few materials of this kind are known. Here we consider ferroelectric/paraelectric superlattices as artificial electrostatically-engineered antiferroelectrics. Specifically, using high-throughput second-principles calculations, we engineer $PbTiO_3$/$SrTiO_3$ superlattices to optimize their energy-storage performance at room temperature (to maximize density and release efficiency) with respect to different design variables (layer thicknesses, epitaxial conditions, stiffness of the dielectric layer). We obtain results competitive with the state-of-the-art antiferroelectric capacitors and reveal the mechanisms responsible for the optimal properties.

Introduction

One of the limiting factors in the miniaturization of present day electronics is the relatively large size of their capacitors, due to their somewhat low energy density. Antiferroelectric materials could help solve this problem[1,2]. These compounds present an antipolar structure of electric dipoles, yielding overall no net polarization P. Yet, applying a large enough electric field ε can switch the system onto a polar state of large polarization (see Fig. 1). The energy density required to charge the system in this way (W_{in}) is proportional to the area to the left of the charging branch in the P-ε loop, which is indicated in purple in Fig. 1. Upon removal of the electric field the released energy density is proportional to the area to the left of the discharge branch (W_{out}, in green in the figure). The energy loss (L) is therefore proportional to the area enclosed by the loop in the P-ε diagram (red-shaded area in Fig. 1). This field-driven phase transition can be utilized in a capacitor with possible applications in pulsed power technologies[3]. Still, relatively few antiferroelectrics are known[2], which hampers the optimization of the effect. Hence, there is a pressing need to discover new antiferroelectric materials.

In the past years, several efforts have been devoted to improving the energy-storing performance of known antiferroelectrics. Polymers and ceramic/polymer composites can present high breakdown fields, but store modest energy densities and typically suffer from poor thermal stability[4,5]. Several works have reported noticeable energy densities in samples of hafnia- and zirconia-based antiferroelectrics[6–10], although with modest efficiency W_{out}/W_{in} due to a strong hysteretic behaviour. A more promising route explored by many groups is chemical substitution in antiferroelectric perovskites[11–22]. To our best knowledge, the highest energy density in an antiferroelectric experimentally achieved to date is 154 J cm^{-3} and corresponds to a complex perovskite solid solution[17].

Several works have found or predicted antiferroelectric-ity in electrostatically frustrated perovskite oxides. Antiferroelectric phases were measured in $KNbO_3$/$KTaO_3$[23] and $SrTiO_3$/$BaZrO_3$[24] superlattices, though the former present scant thermal stability, and the latter display antiferroelectricity for very thin layers. Theoretical works have predicted the appearance of antipolar states in $BaTiO_3$/BaO superlattices[25] (though the electric field response was not computed) or electrostatically engineered ferroelectric thin films[26] (which display small stability regions). Still, the measured or predicted stability windows in these systems are rather narrow, leaving little room for optimization.

In the last years, multidomain structures have been reported in $PbTiO_3$/$SrTiO_3$ superlattices[27–29]. The observed dipole structures can be deemed antipolar, and hence these systems are good candidates to display antiferroelectric-like behaviour. These superlattices have attracted attention lately since they have been found to host negative capacitance[30], non-trivial dipole topologies[29,31,32], and subterahertz collective dynamics[33], with possible applications for voltage amplification and in electric-field-driven data processing, among others.

In this work we test the performance of ferroelectric/paraelectric superlattices as artificial antiferroelectrics for energy storage, taking $PbTiO_3$/$SrTiO_3$ as a relevant model system. We show that the antipolar multidomain state of these heterostructures can be switched to a monodomain polar one under an electric field, yielding response curves similar to that of Figure 1, and thus displaying antiferroelectric-like behaviour. These superlattices offer multiple design variables, including the $PbTiO_3$ and $SrTiO_3$ layer thicknesses, the epitaxial strain imposed by a substrate, or the stiffness of the dielectric layer (which can be controlled through its composition), which are expected to have a significant impact in their electrostatic response and thus in its performance as capacitors. We explore these optimization possibilities by using second-principles simulation methods (which have
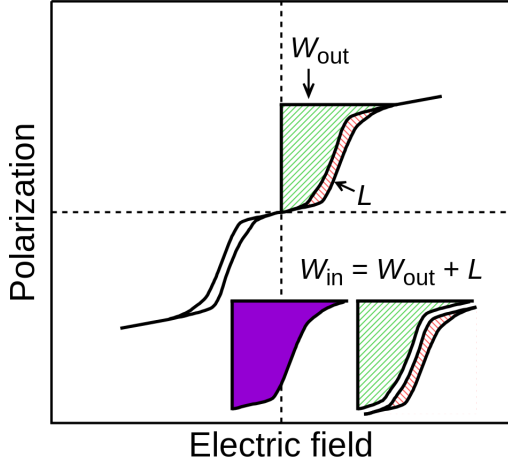
FIG. 1. Energy storage in P-ε loops. The energy density required to charge the system (W_{in}) is equal to the recovered energy density upon discharge (W_{out}) plus the loss (L). Energy densities are proportional to areas in P-ε diagrams.

proven successful to describe these superlattices in previous works[29,30,34]) to run a high-throughput investigation over these design variables. We also reveal the underlying physics yielding the best properties.

Results

In ferroelectric/paraelectric superlattices with the polarization easy axis along the growth direction, the development of a homogeneous polar state in the ferroelectric layer is hindered by the electrostatic penalty due to the surrounding dielectric layers. This often results in the ferroelectric component breaking into domains with opposite local polarizations, as shown in Figure 2. The resulting state can be regarded as antipolar.

Let us consider $(\text{PbTiO}_3)_m/(\text{SrTiO}_3)_n$ superlattices, where m and n are the thicknesses (in perovskite unit cells) of the PbTiO$_3$ and SrTiO$_3$ layers, respectively, and let us take the $(\text{PbTiO}_3)_4/(\text{SrTiO}_3)_4$ system as a representative case for the following discussion. In Figure 2**a** we show the lowest energy dipole configuration obtained for this material using second principles. It presents domains with polarization along the growth direction (z), yielding an overall antipolar structure. The phonon spectrum (Figure 2**b**) of the high-symmetry superlattice state (in which all the atoms are fixed to the ideal high-symmetry perovskite positions) presents a leading antipolar instability (Figure 2**c**), but also homogeneous polar instabilities with in-plane (Figure 2**d**) and out-of-plane (Figure 2**e**) polarizations. It is thus expected that an electric field along the stacking direction could stabilize a monodomain configuration corresponding to Figure 2**e**.

This type of dipole structure was predicted by first-principles[35], second-principles[30] (like those used in this work), and phase-field[36] simulations, and was also experimentally observed[28,37]. Similar multidomain states have
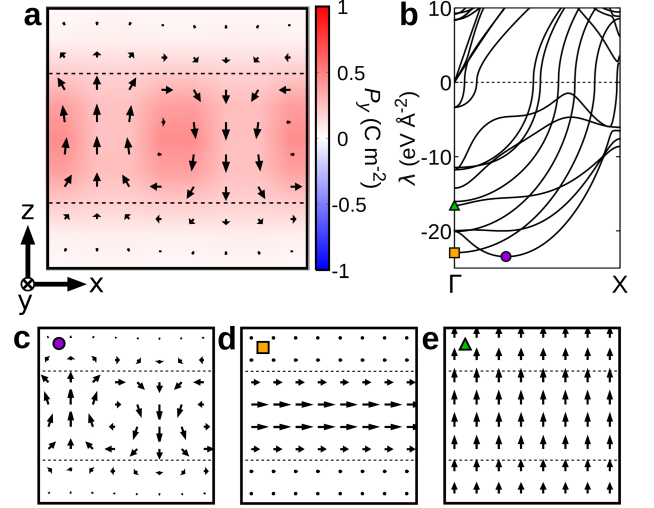

FIG. 2. **a** Lowest energy state of the $(\text{PbTiO}_3)_4/(\text{SrTiO}_3)_4$ superlattice. **b** Phonon instabilities of the high-symmetry $(\text{PbTiO}_3)_4/(\text{SrTiO}_3)_4$ superlattice (in which the atoms in the PbTiO$_3$ and SrTiO$_3$ layers are in the cubic phase) along the $\Gamma - X$ direction. The eigenvectors of the leading instability (purple circle) and two relevant polar instabilities (orange square and green triangle) are shown in the panels below. **c**, **d**, and **e** depict the eigenvectors for the phonons marked with the corresponding symbols in **b**. In panels **a**, **c**, **d** and **e** the arrows indicate the atomic dipoles, and the out of screen component of the dipoles is colour coded according to the scale shown in **a**.

also been reported for BaTiO$_3$/SrTiO$_3$ superlattices in the past years[38–40].

We make use of Monte Carlo simulations under electric field (see Methods) to compute polarization–electric field diagrams for these systems. In Figure 3**a** we show the response of the $(\text{PbTiO}_3)_4/(\text{SrTiO}_3)_4$ superlattice at low temperatures (strictly, 0 K). The material presents the mentioned antipolar state at zero field, and undergoes a field-induced phase transition onto a polar state for fields of a few MV cm^{-1}. This transition occurs in steps (corresponding to the switching of dipole columns in the ferroelectric layer) and is slightly hysteretic. Our calculations thus predict that these superlattices display antiferroelectric-like behaviour.

In Figure 3**b** we show the results of a similar calculation at room temperature. It is apparent that the polarization at high fields decreases with respect to the low temperature result, and that the switching is smoother and non-hysteric. More importantly, even if a static antipolar character at zero field is not apparent in instantaneous configurations (see snapshot of the system in inset to the left of Figure 3**b**), the thermal average of the polarization is clearly still zero. At large fields the superlattice does present a clear polar order, as shown in the representative system snapshot to the right of Figure 3**b**. This indicates that the antiferroelectric-like behaviour is preserved at ambient conditions, which makes PbTiO$_3$/SrTiO$_3$ superlattices a promising playground
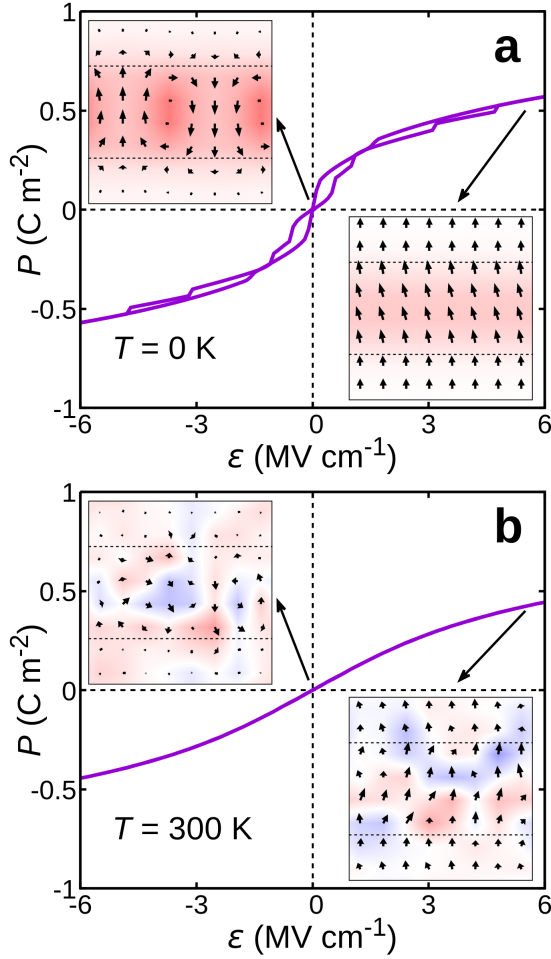
FIG. 3. Representative P-ε diagrams of PbTiO$_3$/SrTiO$_3$ superlattices at zero Kelvin (**a**) and room temperature (**b**). The insets in **a** show the polarization state at zero field and at saturation. The insets in **b** show representative snapshots of the system at zero field and at saturation. The colour scale for the polarization component perpendicular to the paper is that of Figure 2**a**.

for antiferroelectric capacitors.

We now investigate how the design parameters affect the performance of the $(\mathrm{PbTiO}_3)_m/(\mathrm{SrTiO}_3)_n$ superlattices for energy storage. To this end, we run high-throughput calculations of electric field cycles up to 3.5 MV cm^{-1}, with varying PbTiO$_3$ and SrTiO$_3$ thicknesses (between 2 and 12, and between 2 and 20 perovskite unit cells, respectively), epitaxial strain η (between -3% and $+3\%$, taking an SrTiO$_3$ substrate as the zero of strain), and dielectric stiffness of the SrTiO$_3$ layer. This stiffness can be controlled experimentally by chemical substitution, and we model it by including an additional inter-atomic term (denoted h_{STO}) to favour or penalize polar distortions in SrTiO$_3$ (see Methods). In this way we obtain a database of more than 1250 P-ε curves. We integrate the curves to obtain the stored energy density as a function of the maximum applied field

($\varepsilon_{\mathrm{max}}$), and we compute the zero-field susceptibility (χ_0) and switching field ($\varepsilon_{\mathrm{sw}}$) of each P-ε curve (see Methods) to gain some insight into the results in terms of simple physical descriptors.

In order to identify correlations, we work with parallel coordinates plots[41]. In these plots several vertical axes are displayed in parallel, each representing one physical descriptor. Every considered superlattice is represented by one line in the plot. The lines are coloured according to the energy density at a given maximum field (which is also represented in one of the vertical axes), so that correlations can be visualized more easily. In Figure 4**a** we show the plot in which the colour scale follows the stored energy density for a maximum applied field of 0.5 MV cm^{-1} ($W_{0.5}$). By visual inspection one can see that the best superlattices for $\varepsilon_{\mathrm{max}}$ = 0.5 MV cm^{-1}, shown in red, are those with the largest PbTiO$_3$ to SrTiO$_3$ thickness ratios $R = m/n$, the largest zero-field susceptibilities, and the smallest switching fields. It is also clear from the figure that a good performance at small applied fields essentially implies a relatively poor performance at larger fields. Even the less pronounced correlations of $W_{0.5}$ with dielectrically softer SrTiO$_3$ (negative h_{STO}) and strains between 0 and -3% are also clear from the figure. Similar plots, in which the colour scale represents the stored energy density at 2.0 MV cm^{-1} ($W_{2.0}$), and 3.5 MV cm^{-1} ($W_{3.5}$), are shown in Figures 4**b** and 4**c**, respectively. (For plots colour-coded according to the energy density at intermediate fields see Supplementary Figure S1.)

We find a strong correlation between χ_0 and the energy density for small $\varepsilon_{\mathrm{max}}$ values (see Fig. 4**a**). Note that in this (linear) regime a large χ_0 implies a large polarization response for a small applied field, which in turn translates into a large energy density. As the field increases (and we move into the non-linear regime) we see that the better performing superlattices show lower values of χ_0. A lower χ_0 indicates a flatter initial slope in the P-ε diagram, which is beneficial for large enough $\varepsilon_{\mathrm{max}}$ values (compare for instance the performance of the red and green curves in Figures 1**a** and 1**b**).

We observe that at low fields (Figure 4**a**), a larger R ratio is correlated with a better performance, while at high fields (Figure 4**c**) the opposite holds true. To better understand this behaviour, in Figures 5**a** and 5**b** we show how the variation of R affects the polarization and energy density of representative superlattices: a thicker ferroelectric layer (or, equivalently, a thinner dielectric layer) brings the system closer to the limit of a bulk ferroelectric compound. This leads to a larger polarization in the switched state, which in turn increases the energy density. However, it is also apparent from these figures that this effect comes with a reduction of the switching field, and that, in general, the optimal R will depend on the maximum applied field.

At low fields, the best performing superlattices tend to have dielectrically-soft SrTiO$_3$ layers (negative h_{STO}), although many systems with unmodified stiffness (i.e.

undoped $SrTiO_3$, $h_{STO} = 0$) yield almost equally good performances. A correlation between softened $SrTiO_3$ and high performance is apparent at medium and large applied fields. We analyze in detail the effect of varying h_{STO} in Figures 5c and 5d. We see that a stiffer dielectric layer (positive h_{STO}) imposes a larger electrostatic penalty on the polar phase and hence reduces the high-field polarization, which is detrimental for the energy density. However, it also results in a decrease in the switching field, so that (as it was the case for R) the optimal dielectric stiffness depends on the maximum applied field (see Figure 5d).

A compressive epitaxial strain of up to -3% is found to be correlated with better performances in general. This is specially true for intermediate and large maximum fields, while at low fields the optimal strain window widens and includes unstrained superlattices. The effect of varying the epitaxial strain is illustrated in Figures 5e and 5f. Compressive strain favours the tetragonal distortion of $PbTiO_3$ and hence the alignment of its polarization along the growth direction, yielding overall a larger saturation polarization and increasing the energy density. At -3% strain we observe a flattening of the initial slope in the P-ε curve (i.e. a decrease in χ_0) accompanied with an increase in the switching field (from zero to a finite value). This reflects the fact that the compressive strain yields a more stable multidomain zero-field state with large local polarizations, and therefore a higher energy barrier to escape out of it. Ultimately this results in an increase in the energy density, as shown in Figure 5f. It thus seems that, at least in the studied range of ε_{max}, compressive epitaxial strain always has a positive impact on the stored energy density. This also points to the possibility of further optimizing the superlattices by using a ferroelectric layer with a larger bulk spontaneous polarization.

It is clear from Figure 4 that the highest values of $W_{0.5}$, $W_{2.0}$, and $W_{3.5}$ are respectively correlated with switching fields of 0, just below 2.0 MV cm^{-1} and just below 3.5 MV cm^{-1}. Indeed, we overall find that, given a maximum applied field ε_{max}, the stored energy density is optimal for systems which have a switching field just below the applied field ($\varepsilon_{sw} \lesssim \varepsilon_{max}$). A late switching is beneficial for the stored energy since the area to the left of the P-ε curve will be larger the later the polarization develops (e.g. compare the red and green curves in Figures 5a and 5b). This conclusion is in line with the ideas put forward in Refs. 3 and 42.

Discussion

The $PbTiO_3/SrTiO_3$ superlattices studied in this work present larger energy densities than most of the measured antiferroelectric capacitors. At the highest field considered, $\varepsilon_{max} = 3.5$ MV cm^{-1}, our best superlattices store more than 110 J cm^{-3}, which greatly exceeds the best results for hafnia-based antiferroelectrics (less than 40 J cm^{-3})[6], or relaxor ferroelectric thin films (almost 80 J cm^{-3})[21], and is only surpassed by the complex perovskite solid solution that holds the present record
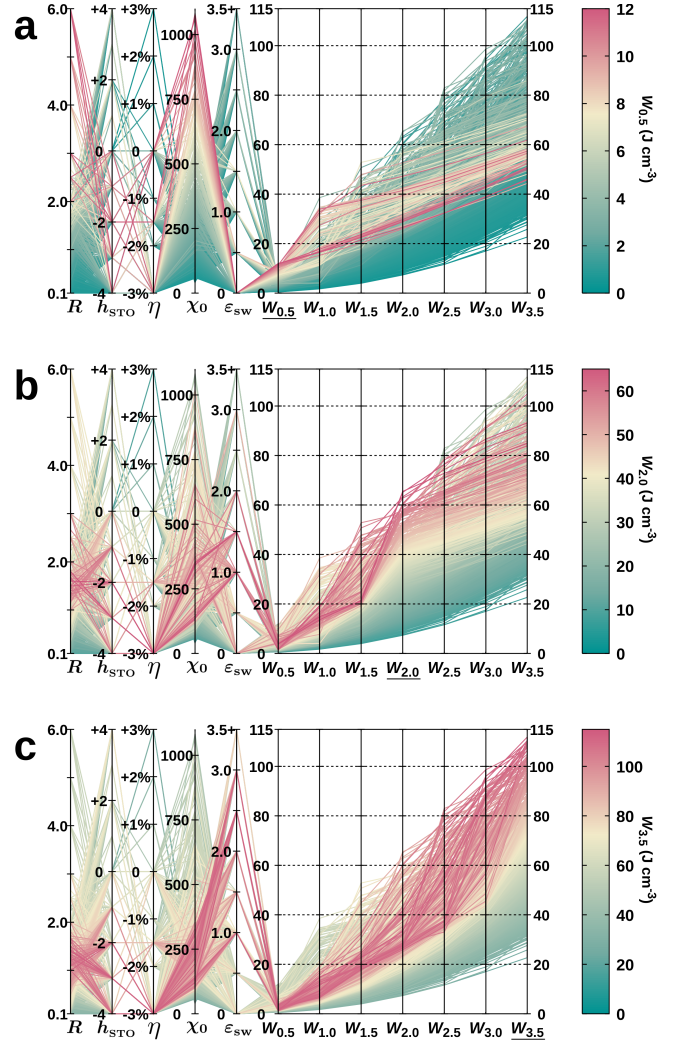

FIG. 4. Parallel coordinates plots of the high-throughput data. The columns, from left to right, correspond respectively to $PbTiO_3/SrTiO_3$ ratio (R), modified $SrTiO_3$ stiffness (h_{STO}), epitaxial strain (η), zero-field susceptibility (χ_0), switching field (ε_{sw}), and stored energy densities at different values of the applied electric field ($W_{0.5}$, $W_{1.0}$, $W_{1.5}$, $W_{2.0}$, $W_{2.5}$, $W_{3.0}$, and $W_{3.5}$). The lines are coloured according to $W_{0.5}$, $W_{2.0}$, and $W_{3.5}$, in panels **a**, **b**, and **c**, respectively (corresponding colour scales to the right of each panel).

$(154$ J cm$^{-3})$[17], to our best knowledge.

If we focus on an intermediate field of $\varepsilon_{max} = 2.0$ MV cm^{-1}, we find maximum energy densities of 65 J cm^{-3}, which is larger than the largest value measured at that field in complex perovskite solid solutions (almost 50 J cm^{-3})[22], relaxor thin films (almost 30 J cm^{-3})[43], or hafnia-based materials (around 10 J cm^{-3})[6].

For the lowest field here considered, $\varepsilon_{max} = 0.5$ MV cm^{-1}, the best $PbTiO_3/SrTiO_3$ superlattice stores 12 J cm^{-3}, very close to the largest experimentally observed value for perovskite solid solutions
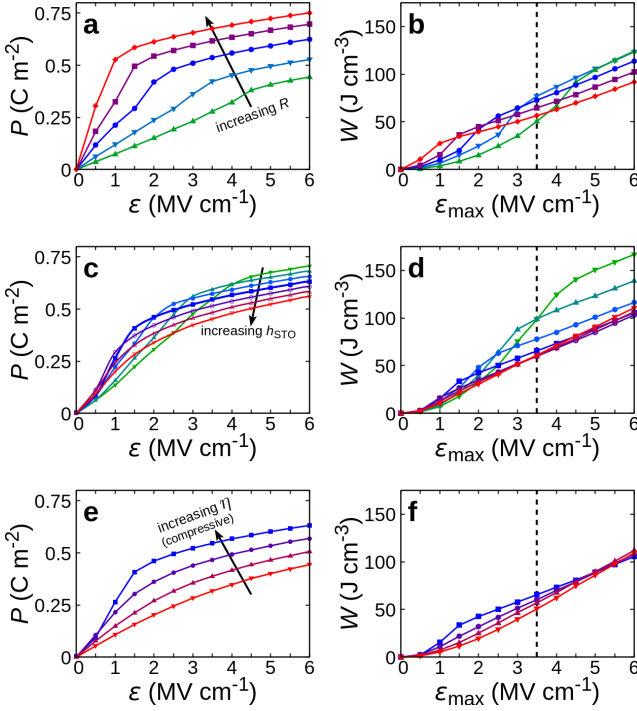
FIG. 5. Effect of the different design parameters on the P-ε loops (left column) and on the stored energy density (right column) **a** and **b** show respectively how the P-ε curves and stored energy density vary with the PbTiO$_3$ to SrTiO$_3$ ratio R. **c** and **d**: same as **a** and **b** for SrTiO$_3$ stiffness. **e** and **f**: same as **a** and **b** for in-plane epitaxial strain η.

(12.6 J cm^{-3})[22], and outperforming the reported relaxor thin films (7.7 J cm^{-3})[11] and hafnia-based materials (below 2 J cm^{-3})[6].

Let us also note that very high energy densities have recently been predicted in AlN/ScN superlattices, up to 135 J cm^{-3} and 200 J cm^{-3} for very large fields of 5.0 MV cm^{-1} and 6.3 MV cm^{-1}, respectively[44]. Still, in the cited work, these fields were rescaled by a factor of 1/3 to match an experimental response curve, so a direct comparison to our results is not possible (the fields actually considered in the simulations of Ref. 44 were of the order of 15 MV cm^{-1}, well beyond typical breakdown fields). Along the same lines, in Ref. 19 lead-free perovskite solid solutions were predicted to display energy-storage performances that exceed our present results; however, electric fields were rescaled by a factor of 1/23 in that work, which complicates a direct comparison.

While the second-principles models employed here have been shown to be qualitatively correct, one may wonder about their quantitative accuracy to reproduce experiments. We can get an idea by comparing our results with the P-ε curve of the (PbTiO$_3$)$_5$/(SrTiO$_3$)$_5$ superlattice reported in Ref. 45; there we find a polarization of around 0.2 C m^{-2} at 0.5 MV cm^{-1}, while our simulations yield a polarization 3 times smaller for the same field. We attribute this to the fact that our

simulated SrTiO$_3$ layers are significantly stiffer than the experimental ones[30]. At any rate, this does not affect the trends and basic quantitative results presented here. Indeed, we could try to reproduce experimentally our simulated superlattices by considering Zr-doped SrTiO$_3$, which should result in relatively stiff dielectric layers.

In conclusion, we have computed the room-temperature energy storage capabilities of over 1000 PbTiO$_3$/SrTiO$_3$ superlattices with different defining parameters. This high-throughput approach (possible thanks to second-principles methods) allows us to identify optimal conditions, predicting that these systems outperform most of the reported antiferroelectric capacitors in a wide range of applied fields. The best materials consistently present a switching field just below the maximum applied field, indicating that tuning this variable is key to improving energy-storing performance. Moreover, we find that these superlattices can be tailored to address specific needs by means of strain, layer thicknesses and dielectric stiffness, depending on the available or desired maximum applied fields. Hence, our results indicate that electrostatically engineered ferroelectric/paraelectric superlattices are promising materials for applications in pulsed power technologies.

Methods

We run second-principles simulations as implemented in the SCALE-UP code[46–48]. The models for the superlattices are derived from models for bulk SrTiO$_3$ and bulk PbTiO$_3$ which have been used in previous works[46,49,50] and give correct descriptions of the lattice dynamical properties of both compounds. Then, as described also in Ref. 29, the interactions involving interfacial atoms in the superlattices are taken as the numerical average of the corresponding interactions in PbTiO$_3$ and SrTiO$_3$. In order to reproduce the correct long-range electrostatic behaviour, an effective dielectric tensor $\epsilon^{\infty,\mathrm{SL}}$ is used for the superlattice. Along the growth direction of the superlattice the system is considered as capacitors in series, so that the inverse of the diagonal component of the electrostatic tensor along the growth direction, $\epsilon_{zz}^{\infty,\mathrm{SL}}$ is taken as the weighted sum of the inverses of the corresponding tensor elements for bulk PbTiO$_3$ ($\epsilon_{zz}^{\infty,\mathrm{PTO}}$) and SrTiO$_3$ ($\epsilon_{zz}^{\infty,\mathrm{PTO}}$) as obtained from first principles, where the weights (t_{PTO} and t_{STO}) are the relative thicknesses of the respective layers of PbTiO$_3$ and SrTiO$_3$:

$$(\epsilon_{zz}^{\infty,\mathrm{SL}})^{-1} = t_{\mathrm{PTO}}(\epsilon_{zz}^{\infty,\mathrm{PTO}})^{-1} + t_{\mathrm{STO}}(\epsilon_{zz}^{\infty,\mathrm{STO}})^{-1} \quad (1)$$

Analogously, for the in-plane components of the electrostatic tensor the layers are considered as capacitors in parallel, resulting in an effective in-plane electrostatic tensor given by:

$$\epsilon_{ii}^{\infty,\mathrm{SL}} = t_{\mathrm{PTO}}\epsilon_{ii}^{\infty,\mathrm{PTO}} + t_{\mathrm{STO}}\epsilon_{ii}^{\infty,\mathrm{STO}} \text{ for } i = x,y \quad (2)$$

Finally, and in order to recover the correct bulk limits, the Born effective charges ($Z_\alpha^{*,\mathrm{SL}}$, where α runs through the atoms) within each layer j are rescaled by

$\sqrt{\epsilon^{\infty,\mathrm{SL}}/\epsilon^{\infty,j}}$ where j= PTO, STO. For the Ti and O atoms at the interfaces the Born effective charges are renormalized as follows: $Z^*_\alpha = \frac{1}{2}\sqrt{\epsilon^{\infty,\mathrm{SL}}/\epsilon^{\infty,j}}Z^{*,\mathrm{PTO}}_\alpha + \frac{1}{2}\sqrt{\epsilon^{\infty,\mathrm{SL}}/\epsilon^{\infty,j}}Z^{*,\mathrm{STO}}_\alpha$ where $Z^{*,\mathrm{PTO}}_\alpha$ and $Z^{*,\mathrm{STO}}_\alpha$ are the Born effective charges of atom α in bulk PbTiO$_3$ and SrTiO$_3$, respectively, and α= Ti, O at the interface.

The second-principles parameters of both materials are fitted from density functional theory calculations at a hydrostatic pressure of -11.2 GPa to correct for the underestimation due to the local density approximation of the cubic lattice constant that is taken as the reference structure.

The dielectric stiffness of the SrTiO$_3$ layer is modified by adding an extra interatomic term to the superlattice model, with the representative term $(\mathrm{Ti}_z\text{-}\mathrm{O}_z)^2$, that only affects Ti and O atoms in the SrTiO$_3$ subsystem. (Note that this expression is merely the representation of a symmetry-adapted term[46] but also affects polar distortions in SrTiO$_3$ along the x and y directions.) In this way, a positive coefficient translates into an additional energy cost of polarizing the SrTiO$_3$ layer (and hence the superlattice) in the growth direction. In the high-throughput calculations the coefficient for this term, h_{STO}, is varied between -4 meV Å^{-2} and $+4$ meV Å^{-2}.

For the ground state calculations and the simulation of the zero Kelvin P-ε diagrams we run Monte Carlo simulated annealings for 30000 steps, with an initial temperature of 10 K and an annealing rate of 0.9975. To simulate electric field cycles, the studied electric field range (0 to 6 MV cm^{-1} in Figures 3 and 5, 0 to 3.5 MV cm^{-1} in the high-throughput calculations) is divided in increments of equally length (of 0.2 MV cm^{-1} everywhere, except for the high-throughput calculations for which an electric field step of 0.5 MV cm^{-1} was employed). For each value of the electric field a Monte Carlo simulation is performed sequentially (an annealing for the zero Kelvin diagrams, and a constant temperature Monte Carlo simulation for the finite temperature simulations), using as initial configuration that of the previous step in the electric field ramp. To generate the finite temperature P-ε curves we run Monte Carlo simulations at constant temperature for 30000 steps at each value of the electric field, which we find to be enough to show converged results. The averages of the polarization at each value of the electric field are taken disregarding the initial 5000 steps of each simulation, to allow for thermalization.

The high-throughput calculations are performed in a simulation cell of $8\times2\times1$, where the unitary cell is defined as a 1×1 perovskite unit cells in the xy plane and a full superlattice period in the third direction. We check the convergence of our calculations with respect to the simulation cell. To this end, we compare the P-ε curves of the (PbTiO$_3$)$_4$/(SrTiO$_3$)$_4$ in simulation cells of $8\times2\times1$, $8\times8\times1$ and $12\times12\times1$, both under strains of 0% and -3% (see Supplementary Figure S2). We find that the results for the $8\times8\times1$ cell are very well converged, since they are essentially identical to those of the $12\times12\times1$ cell. The $8\times2\times1$ cell also yields very well converged results under no strain. Under compressive strain the switching field (inflection point of the curve) becomes finite and the results for the $8\times2\times1$ cell are not so well converged around $\varepsilon_{\mathrm{sw}}$. Still, the effect is not very large, and the polarization is underestimated at lower fields, then overestimated at intermediate fields, and finally well converged for high fields. Overall, the effect in the stored energy density is not large (specially for fields above $\varepsilon_{\mathrm{sw}}$).

For a given electric field ramp the zero-field susceptibility χ_0 is computed using finite differences. The switching field is defined as the inflection point in the P-ε curves. In order to estimate the $\varepsilon_{\mathrm{sw}}$ in the P-ε curves we compute their second derivatives using central finite differences and we set $\varepsilon_{\mathrm{sw}}$ to the largest field for which the second derivative is positive (positive curvature). In the cases where the curvature of the P-ε curve is found to be negative for all the studied electric fields, $\varepsilon_{\mathrm{sw}}$ is set to zero. When the curvature is found to be positive for the full range of electric field studied (up to 3.5 MV cm^{-1}), since the large field behaviour has to be that of a saturating polarization with negative polarization, we set the $\varepsilon_{\mathrm{sw}}$ to be 3.5 MV cm^{-1} or more (3.5+ in Figures 4 and S1).

The stored energy density at each value of the field is computed by trapezoid integration of the P-ε over the P axis.

In the high-throughput calculations, we run a full charge-discharge cycle (from zero to 3.5 MV cm^{-1}, then back to zero field) for several sets of design parameters (more than 50) to test for possible hysteresis, finding that none of the systems presented hysteric behaviour.

Author Contributions. J.Í. conceived the research. H.A. performed the calculations and created the figures. All authors contributed to the discussion and analysis of the results. The manuscript was written by H.A. and J.Í., with contributions from N.S.F.

Competing Interests. The authors declare that they have no competing financial interests.

Data availability: Data related to this work is available from the authors upon reasonable request.

[1] L. Zhu, Q. Wang, Novel ferroelectric polymers for high energy density and low loss dielectrics. *Macromolecules* **45**, 2937–2954 (2012).

[2] K. M. Rabe, *Antiferroelectricity in Oxides: A Reexamination* (John Wiley & Sons, Ltd, 2013), chap. 7, pp. 221–244.

[3] I. Burn, D. Smyth, Energy storage in ceramic dielectrics. *Journal of Materials Science* **7**, 339–343 (1972).

[4] H. Gong, B. Miao, X. Zhang, J. Lu, Z. Zhang,

High-field antiferroelectric-like behavior in uniaxially stretched poly (vinylidene fluoride-trifluoroethylene-chlorotrifluoroethylene)-grafted-poly (methyl methacrylate) films with high energy density. *RSC Advances* **6**, 1589–1599 (2016).

[5] L. Li, B. Zhou, J. Ye, W. Wu, F. Wen, Y. Xie, P. Bass, Z. Xu, L. Wang, G. Wang, Z. Zhang, Enhanced dielectric and energy-storage performance of nanocomposites using interface-modified anti-ferroelectric fillers. *Journal of Alloys and Compounds* **831**, 154770 (2020).

[6] M. H. Park, H. J. Kim, Y. J. Kim, T. Moon, K. D. Kim, C. S. Hwang, Thin $Hf_xZr_{1-x}O_2$ films: a new lead-free system for electrostatic supercapacitors with large energy storage density and robust thermal stability. *Advanced Energy Materials* **4**, 1400610 (2014).

[7] M. Pešić, M. Hoffmann, C. Richter, T. Mikolajick, U. Schroeder, Nonvolatile random access memory and energy storage based on antiferroelectric like hysteresis in ZrO_2. *Advanced Functional Materials* **26**, 7486–7494 (2016).

[8] L. Zhang, M. Liu, W. Ren, Z. Zhou, G. Dong, Y. Zhang, B. Peng, X. Hao, C. Wang, Z.-D. Jiang, W. Jing, Z.-G. Ye, ALD preparation of high-k HfO_2 thin films with enhanced energy density and efficient electrostatic energy storage. *RSC Advances* **7**, 8388–8393 (2017).

[9] S. J. Kim, J. Mohan, J. S. Lee, H. S. Kim, J. Lee, C. D. Young, L. Colombo, S. R. Summerfelt, T. San, J. Kim, Stress-induced crystallization of thin $Hf_{1-x}Zr_xO_2$ films: The origin of enhanced energy density with minimized energy loss for lead-free electrostatic energy storage applications. *ACS Applied Materials & Interfaces* **11**, 5208–5214 (2019).

[10] S.-H. Yi, H.-C. Lin, M.-J. Chen, Ultra-high energy storage density and scale-up of antiferroelectric $TiO_2/ZrO_2/TiO_2$ stacks for supercapacitors. *Journal of Materials Chemistry A* **9**, 9081–9091 (2021).

[11] B. Ma, D.-K. Kwon, M. Narayanan, U. B. Balachandran, Dielectric properties and energy storage capability of antiferroelectric $Pb_{0.92}La_{0.08}Zr_{0.95}Ti_{0.05}O_3$ film-on-foil capacitors. *Journal of Materials Research* **24**, 2993–2996 (2009).

[12] B. Ma, M. Narayanan, U. B. Balachandran, Dielectric strength and reliability of ferroelectric PLZT films deposited on nickel substrates. *Materials Letters* **63**, 1353–1356 (2009).

[13] M. Ye, Q. Sun, X. Chen, Z. Jiang, F. Wang, Effect of eu doping on the electrical properties and energy storage performance of $PbZrO_3$ antiferroelectric thin films. *Journal of the American Ceramic Society* **94**, 3234–3236 (2011).

[14] K. Yao, S. Chen, M. Rahimabady, M. S. Mirshekarloo, S. Yu, F. E. H. Tay, T. Sritharan, L. Lu, Nonlinear dielectric thin films for high-power electric storage with energy density comparable with electrochemical supercapacitors. *IEEE transactions on ultrasonics, ferroelectrics, and frequency control* **58**, 1968–1974 (2011).

[15] X. Hao, J. Zhou, S. An, Effects of PbO content on the dielectric properties and energy storage performance of $(Pb_{0.97}La_{0.02})(Zr_{0.97}Ti_{0.03})O_3$ antiferroelectric thin films. *Journal of the American Ceramic Society* **94**, 1647–1650 (2011).

[16] Z. Hu, B. Ma, R. Koritala, U. Balachandran, Temperature-dependent energy storage properties of antiferroelectric $Pb_{0.96}La_{0.04}Zr_{0.98}Ti_{0.02}O_3$ thin films. *Applied Physics Letters* **104**, 263902 (2014).

[17] B. Peng, Q. Zhang, X. Li, T. Sun, H. Fan, S. Ke, M. Ye, Y. Wang, W. Lu, H. Niu, J. F. Scott, X. Zeng, H. Huang, Giant electric energy density in epitaxial lead-free thin films with coexistence of ferroelectrics and antiferroelectrics. *Advanced Electronic Materials* **1**, 1500052 (2015).

[18] C. W. Ahn, G. Amarsanaa, S. S. Won, S. A. Chae, D. S. Lee, I. W. Kim, Antiferroelectric thin-film capacitors with high energy-storage densities, low energy losses, and fast discharge times. *ACS Applied Materials & Interfaces* **7**, 26381–26386 (2015).

[19] B. Xu, J. Íñiguez, L. Bellaiche, Designing lead-free antiferroelectrics for energy storage. *Nature Communications* **8**, 1–8 (2017).

[20] H. Pan, F. Li, Y. Liu, Q. Zhang, M. Wang, S. Lan, Y. Zheng, J. Ma, L. Gu, Y. Shen, P. Yu, S. Zhang, L.-Q. Chen, Y.-H. Lin, C.-W. Nan, Ultrahigh–energy density lead-free dielectric films via polymorphic nanodomain design. *Science* **365**, 578–582 (2019).

[21] J. Kim, S. Saremi, M. Acharya, G. Velarde, E. Parsonnet, P. Donahue, A. Qualls, D. Garcia, L. W. Martin, Ultrahigh capacitive energy density in ion-bombarded relaxor ferroelectric films. *Science* **369**, 81–84 (2020).

[22] Y. Z. Li, J. L. Lin, Y. Bai, Y. Li, Z. D. Zhang, Z. J. Wang, Ultrahigh-energy storage properties of $(PbCa)ZrO_3$ antiferroelectric thin films via constructing a pyrochlore nanocrystalline structure. *ACS Nano* **14**, 6857–6865 (2020).

[23] J. Sigman, D. Norton, H. Christen, P. Fleming, L. Boatner, Antiferroelectric behavior in symmetric $KNbO_3/KTaO_3$ superlattices. *Physical Review Letters* **88**, 097601 (2002).

[24] H. M. Christen, E. D. Specht, S. S. Silliman, K. S. Harshavardhan, Ferroelectric and antiferroelectric coupling in superlattices of paraelectric perovskites at room temperature. *Physical Review B* **68**, 020101 (2003).

[25] E. Bousquet, J. Junquera, P. Ghosez, First-principles study of competing ferroelectric and antiferroelectric instabilities in $BaTiO_3/BaO$ superlattices. *Physical Review B* **82**, 045426 (2010).

[26] E. Glazkova, K. McCash, C.-M. Chang, B. Mani, I. Ponomareva, Tailoring properties of ferroelectric ultrathin films by partial charge compensation. *Applied Physics Letters* **104**, 012909 (2014).

[27] P. Zubko, N. Stucki, C. Lichtensteiger, J.-M. Triscone, X-ray diffraction studies of 180 ferroelectric domains in $PbTiO_3/SrTiO_3$ superlattices under an applied electric field. *Physical Review Letters* **104**, 187601 (2010).

[28] A. Yadav, C. Nelson, S. Hsu, Z. Hong, J. Clarkson, C. Schlepütz, A. Damodaran, P. Shafer, E. Arenholz, L. Dedon, , D. Chen, A. Vishwanath, A. Minor, L. Chen, J. Scott, L. Martin, R. Ramesh, Observation of polar vortices in oxide superlattices. *Nature* **530**, 198–201 (2016).

[29] S. Das, Y. Tang, Z. Hong, M. A. P. Gonçalves, M. McCarter, C. Klewe, K. Nguyen, F. Gómez-Ortiz, P. Shafer, E. Arenholz, V. Stoica, S.-L. Hsu, B. Wang, C. Ophus, J. F. Liu, C. T. Nelson, S. Saremi, B. Prasad, A. B. Mei, D. Schlom, J. Íñiguez, P. García-Fernández, D. A. Muller, L. Q. Chen, J. Junquera, L. W. Martin, R. Ramesh, Observation of room-temperature polar skyrmions. *Nature* **568**, 368–372 (2019).

[30] P. Zubko, J. C. Wojdeł, M. Hadjimichael, S. Fernandez-Pena, A. Sené, I. Luk'yanchuk, J.-M. Triscone, J. Íñiguez, Negative capacitance in multidomain ferroelectric superlattices. *Nature* **534**, 524–528 (2016).

[31] M. A. P. Gonçalves, C. Escorihuela-Sayalero, P. García-Fernández, J. Junquera, J. Íñiguez, Theoretical guidelines to create and tune electric skyrmion bubbles. *Science Advances* **5**, eaau7023 (2019).

[32] A. Y. Abid, Y. Sun, X. Hou, C. Tan, X. Zhong, R. Zhu, H. Chen, K. Qu, Y. Li, M. Wu, J. Zhang, J. Wang, K. Liu, X. Bai, D. Yu, X. Ouyang, J. Wang, J. Li, P. Gao, Creating polar antivortex in PbTiO$_3$/SrTiO$_3$ superlattice. *Nature Communications* **12**, 1–7 (2021).

[33] Q. Li, V. A. Stoica, M. Paściak, Y. Zhu, Y. Yuan, T. Yang, M. R. McCarter, S. Das, A. K. Yadav, S. Park, C. Dai, H. J. Lee, Y. Ahn, S. D. Marks, S. Yu, C. Kadlec, T. Sato, M. C. Hoffmann, M. Chollet, M. E. Kozina, S. Nelson, D. Zhu, D. A. Walko, A. M. Lindenberg, P. G. Evans, L.-Q. Chen, R. Ramesh, L. W. Martin, V. Gopalan, J. W. Freeland, J. Hlinka, H. Wen, Subterahertz collective dynamics of polar vortices. *Nature* **592**, 376–380 (2021).

[34] A. K. Yadav, K. X. Nguyen, Z. Hong, P. García-Fernández, P. Aguado-Puente, C. T. Nelson, S. Das, B. Prasad, D. Kwon, S. Cheema, A. I. Khan, C. Hu, J. Íñiguez, J. Junquera, L.-Q. Chen, D. A. Muller, R. Ramesh, S. Salahuddin, Spatially resolved steady-state negative capacitance. *Nature* **565**, 468–471 (2019).

[35] P. Aguado-Puente, J. Junquera, Structural and energetic properties of domains in PbTiO$_3$/SrTiO$_3$ superlattices from first principles. *Physical Review B* **85**, 184105 (2012).

[36] Q. Li, C. Nelson, S.-L. Hsu, A. Damodaran, L.-L. Li, A. Yadav, M. McCarter, L. Martin, R. Ramesh, S. Kalinin, Quantification of flexoelectricity in PbTiO$_3$/SrTiO$_3$ superlattice polar vortices using machine learning and phase-field modeling. *Nature Communications* **8**, 1–8 (2017).

[37] P. Chen, X. Zhong, J. A. Zorn, M. Li, Y. Sun, A. Y. Abid, C. Ren, Y. Li, X. Li, X. Ma, J. Wang, K. Liu, Z. Xu, C. Tan, L. Chen, P. Gao, X. Bai, Atomic imaging of mechanically induced topological transition of ferroelectric vortices. *Nature Communications* **11**, 1–8 (2020).

[38] S. Lisenkov, L. Bellaiche, Phase diagrams of BaTiO$_3$/SrTiO$_3$ superlattices from first principles. *Phys. Rev. B* **76**, 020102 (2007).

[39] S. Estandía, F. Sánchez, M. F. Chisholm, J. Gázquez, Rotational polarization nanotopologies in BaTiO$_3$/SrTiO$_3$ superlattices. *Nanoscale* **11**, 21275–21283 (2019).

[40] D. Peng, X. Yang, W. Jiang, Three-dimensional polarization vortex configuration evolution in compressed BaTiO$_3$/SrTiO$_3$ superlattice. *Journal of Applied Physics* **126**, 244101 (2019).

[41] A. Inselberg, The plane with parallel coordinates. *The Visual Computer* **1**, 69–91 (1985).

[42] S. Liu, Y. Liu, T. Yang, Tailoring switching field of phase transition for enhancing energy-storage density of PLZST antiferroelectric thick films. *Journal of Alloys and Compounds* **861**, 158559 (2021).

[43] B. Ma, Z. Hu, R. E. Koritala, T. H. Lee, S. E. Dorris, U. Balachandran, PLZT film capacitors for power electronics and energy storage applications. *Journal of Materials Science: Materials in Electronics* **26**, 9279–9287 (2015).

[44] Z. Jiang, B. Xu, H. Xiang, L. Bellaiche, Ultrahigh energy storage density in epitaxial AlN/ScN superlattices. *Physical Review Materials* **5**, L072401 (2021).

[45] P. Zubko, N. Jecklin, N. Stucki, C. Lichtensteiger, G. Rispens, J.-M. Triscone, Ferroelectric domains in PbTiO$_3$/SrTiO$_3$ superlattices. *Ferroelectrics* **433**, 127–137 (2012).

[46] J. C. Wojdeł, P. Hermet, M. P. Ljungberg, P. Ghosez, J. Íñiguez, First-principles model potentials for lattice-dynamical studies: General methodology and example of application to ferroic perovskite oxides. *Journal of Physics: Condensed Matter* **25**, 305401 (2013).

[47] P. García-Fernández, J. C. Wojdeł, J. Íñiguez, J. Junquera, Second-principles method for materials simulations including electron and lattice degrees of freedom. *Physical Review B* **93**, 195137 (2016).

[48] C. Escorihuela-Sayalero, J. C. Wojdeł, J. Íñiguez, Efficient systematic scheme to construct second-principles lattice dynamical models. *Physical Review B* **95**, 094115 (2017).

[49] J. C. Wojdeł, J. Íñiguez, Ferroelectric transitions at ferroelectric domain walls found from first principles. *Physical Review Letters* **112**, 247603 (2014).

[50] J. A. Seijas-Bellido, C. Escorihuela-Sayalero, M. Royo, M. P. Ljungberg, J. C. Wojdeł, J. Íñiguez, R. Rurali, A phononic switch based on ferroelectric domain walls. *Physical Review B* **96**, 140101 (2017).